

# Acoustic wave sparsely activated localization microscopy (AWSALM): Super-resolution ultrasound imaging using acoustic activation and deactivation of nanodroplets

Ge Zhang,<sup>1</sup> Sevan Harput,<sup>1</sup> Shengtao Lin,<sup>1</sup> Kirsten Christensen-Jeffries,<sup>2</sup> Chee Hau Leow,<sup>1</sup> Jemma Brown,<sup>2</sup> Christopher Dunsby,<sup>3,a)</sup> Robert J. Eckersley,<sup>2,a)</sup> and Meng-Xing Tang<sup>1,a),b)</sup>

<sup>1</sup>Department of Bioengineering, Imperial College London, London SW7 2AZ, United Kingdom

<sup>2</sup>Biomedical Engineering Department, School of Biomedical Engineering and Imaging Sciences, Kings College London, London SE1 7EH, United Kingdom

<sup>3</sup>Department of Physics and Centre for Pathology, Imperial College London, London SW7 2AZ, United Kingdom

(Received 16 March 2018; accepted 9 May 2018; published online 2 July 2018)

Photo-activated localization microscopy (PALM) has revolutionized the field of fluorescence microscopy by breaking the diffraction limit in spatial resolution. In this study, “acoustic wave sparsely activated localization microscopy (AWSALM),” an acoustic counterpart of PALM, is developed to super-resolve structures which cannot be resolved by conventional B-mode imaging. AWSALM utilizes acoustic waves to sparsely and stochastically activate decafluorobutane nanodroplets by acoustic vaporization and to simultaneously deactivate the existing vaporized nanodroplets via acoustic destruction. In this method, activation, imaging, and deactivation are all performed using acoustic waves. Experimental results show that sub-wavelength micro-structures not resolvable by standard B-mode ultrasound images can be separated by AWSALM. This technique is flow independent and does not require a low concentration of contrast agents, as is required by current ultrasound super resolution techniques. Acoustic activation and deactivation can be controlled by adjusting the acoustic pressure, which remains well within the FDA approved safety range. In conclusion, this study shows the promise of a flow and contrast agent concentration independent super-resolution ultrasound technique which has potential to be faster and go beyond vascular imaging. © 2018 Author(s). All article content, except where otherwise noted, is licensed under a Creative Commons Attribution (CC BY) license (<http://creativecommons.org/licenses/by/4.0/>). <https://doi.org/10.1063/1.5029874>

Optical super-resolution imaging, using photo-activated localization microscopy (PALM)<sup>1</sup> and stochastic reconstruction microscopy (STORM),<sup>2,3</sup> is capable of resolving intracellular organelles and the plasma membrane at spatial resolutions at and below a few 10s of nanometers. The basic principle of PALM is that a first light pulse will activate a subset of fluorescent proteins in the molecule sample. These fluorescent proteins are then excited and imaged until bleached. A second light pulse is then used to activate a new subset of fluorescent proteins. Each spatially isolated fluorescent region in an image is localized as a localization event. All localization events from all images are then assembled into a super-resolution image. The PALM and STORM techniques have revolutionized fluorescence imaging by breaking the diffraction limit in spatial resolution. However, a key disadvantage of such optical techniques is that biological tissue scatters light significantly which limits their penetration depth in biological tissue and makes *in vivo* imaging difficult. *In-vivo* microstructural changes can be an important indicator for the detection and diagnosis of certain diseases, such as ischemia, peripheral arterial disease,<sup>4</sup> coronary heart disease,<sup>5</sup> and tumor angiogenesis.<sup>6</sup>

Ultrasound is much less scattered by biological tissue than optical radiation and is able to image *in vivo* structures in depth.

Gas-filled microbubble contrast agents are used in clinical ultrasound (US) imaging to improve blood flow signals and have a diameter ranging between 1 and 10  $\mu\text{m}$ .<sup>7</sup> These microbubble contrast agents can resonate within the diagnostic ultrasound imaging frequency range from 1 to 15 MHz and generate stronger acoustic signals than tissue, thus improving the contrast in vascular imaging.<sup>8</sup> However, the associated axial resolution limit and its compromise with penetration depth pose challenges in imaging the microstructures such as microstructure *in vivo*. Inspired by optical super-resolution methods, a low concentration of flowing microbubbles was used to perform ultrasound super-resolution imaging to visualize microvasculature beyond the diffraction limit. Two-dimensional acoustic super-resolution imaging has shown promise in both *in vitro*<sup>9</sup> and *in vivo*<sup>10,11</sup> studies using clinical ultrasound systems and microbubble contrast agents. Three-dimensional acoustic super-resolution imaging has been achieved using different approaches in both *in vitro*<sup>12–14</sup> and *in vivo*<sup>15</sup> studies.

Since microbubbles are in an “activated” state (i.e., visible under ultrasound) at the point of injection current, super-resolution imaging techniques using microbubbles rely on low bubble concentration and sufficient flow. Such restrictions, together with the large size of microbubbles, mean that only vascular flow can be imaged, and for small vessels with slow flow, a longer acquisition time is required for the bubbles to replenish.

Nanodroplet contrast agents have been investigated as a research alternative to microbubble contrast agents.<sup>16–19</sup>

<sup>a)</sup>C. Dunsby, R. J. Eckersley, and M.-X. Tang contributed equally to this work.

<sup>b)</sup>Author to whom correspondence should be addressed: [mengxing.tang@ic.ac.uk](mailto:mengxing.tang@ic.ac.uk)

Nanodroplets are typically in the form of droplets of sub-micron size and have been found to last longer during *in-vivo* circulation compared to microbubbles.<sup>17</sup> The sub-micron size of nanodroplets potentially allows extravasation into cancerous tissue due to its leaky vasculature and enhanced permeability and retention effect.<sup>20</sup> This could be beneficial to cancer extravasation imaging. Moreover, the nanodroplets can be selectively activated, both spatially and temporally, to provide an ultrasound contrast signal.

High-boiling-point nanodroplets for super-resolution photoacoustic imaging<sup>21</sup> have been demonstrated recently. This technique does not depend on flow, but photoacoustic activation via a laser was required, which restricts its penetration depth to regions that can be illuminated optically. Compared to high-boiling-point nanodroplets, low-boiling-point nanodroplets have a much lower activation threshold and can be activated by diagnostic ultrasound pulses at depth.<sup>22</sup>

In this study, we show that a high concentration of low-boiling-point nanodroplets can be sparsely and stochastically activated and then deactivated at will through controlling the ultrasound amplitude applied which remains well within clinical safety limits and thus demonstrate the acoustic counterpart of PALM at depth.

Nanodroplet preparation was adapted from previously described methods.<sup>23,24</sup> Briefly, a lipid colloid was generated by dissolving a 9:1 molar ratio of 1,2-dipalmitoyl-sn-glycero-3-phosphocholine (DPPC) and 1,2-distearoyl-sn-glycero-3-phosphoethanolamine-N-[amino(polyethylene glycol)-2000] (DSPE-PEG-2000) into a solution of phosphate-buffered saline (PBS), propylene glycol, and glycerol (16:3:1, v: v) to achieve a total lipid concentration of 1 mg/ml. All the lipids described above were purchased from Avanti Polar Lipids, Inc., USA. A volume of 1 ml of lipid solution was added to a 2 ml glass vial. The headspace of the vial was filled with decafluorobutane gas (Fluoromed, USA) via an inlet needle along with a vent needle. Mechanical agitation was applied using a bubble shaker (Vialmix, USA) to produce the stable and microscale bubbles composed of a gaseous decafluorobutane core encapsulated by a lipid shell.

In order to condense microbubbles into nanodroplets, the headspace of the vial was pressurized according to the previously described methods. The vial of microbubbles was immersed in an ice-salt bath ( $-5^{\circ}\text{C}$  to  $-10^{\circ}\text{C}$ ) followed by pressurization with ambient air into the vial septum while the vial contents remained in the ice-salt bath.

A NanoSight NS300 (Malvern Instruments Ltd., UK) was used to measure the size and concentration of nanodroplet solutions via nanoparticle tracking analysis (NTA), with the nanoparticle size measurement range from 10 to 1000 nm. According to the measurement, the mean diameter was  $118.7 \pm 6.7$  nm and the mean concentration was  $(3.51 \pm 0.26) \times 10^{10}$  droplets/ml.

A crossed-tube phantom was fixed and immersed in a water tank where the walls were covered with acoustic absorbers. The crossed-tube phantom was made of two 200- $\mu\text{m}$ -cellulose tubes (Hemophan®, Membrana) separated by  $30^{\circ}$ . The tube is a thin-walled cellulose capillary tube of an internal diameter of  $200 \pm 15$   $\mu\text{m}$ , a wall thickness of  $8 \pm 1$   $\mu\text{m}$  in the dry state, and a length change under wet

conditions of  $\pm 1\%$  (specifications provided by the manufacturer). An L11-4v transducer equipped with ultrasound research platform (Verasonics Vantage 128, Kirkland, USA) was held 15 mm above the center of the crossed-tubes. The water temperature was maintained at  $37^{\circ}\text{C}$ . A diluted PCCA solution ( $\sim 1.75 \times 10^8$  PCCAs/ml) was prepared in a beaker at  $37^{\circ}\text{C}$ . A magnetic stirrer was put into the beaker for mixing.

The ultrasound imaging system was characterized by measuring the diffraction limited resolution and localization precision. A 50  $\mu\text{m}$  diameter tube was fixed horizontally in a water tank to imitate a point scatterer as described in the previous literature.<sup>10</sup> This was performed at depths of between 1 and 2 cm from the transducer face to test the changes in point spread function (PSF) over the imaging depth. The resolution of the ultrasound imaging system was measured as the mean value of full-width-half-maximum (FWHM) over 100 frames in the lateral and axial directions. The localization precision was measured to be the standard deviation of the measured center of mass over 100 frames. Figures 1(a)–1(c) show a representative image of tube cross-section at a depth of 2 cm. The axial and lateral resolution was measured as a FWHM of 560  $\mu\text{m}$  and 640  $\mu\text{m}$ , respectively.

A customized continuous “Activation-Imaging” sequence was developed and implemented on the ultrasound research platform with an L11-4 linear array probe. The parameters of the ultrasound pulses used are summarized in Table I. A sequence of 128 2-cycle, 8 MHz focused pulses were transmitted at a mechanical index of 1.30 in order to sparsely activate the nanodroplet population. One-cycle, 4 MHz plane-wave pulses were then used to acquire images of the vaporized nanodroplets at a mechanical index of 0.25.

As illustrated in Figs. 1(d)–1(g), thirty (30) post-activation images were acquired at a frame rate of 100 frames per second after each activation pulse sequence. Each activation pulse sequence consists of 128 focused activation pulses and it took 1.247 ms to scan the focus across the field of view at a depth of 15 mm. The data acquisition period was 30 s. The received radiofrequency (RF) signals were reconstructed using a delay-and-sum (DAS) beamformer previously demonstrated in Ref. 25. Singular value decomposition (SVD) processing was used in order to obtain the activated nanodroplet signals without the background signal.<sup>26</sup>

After SVD processing, the ultrasound image frames were envelope detected. Super-localization was performed on each ultrasound image after setting an image pixel value threshold to reject the noise and detect potential vaporized droplets. Each detected event in the image after thresholding was compared to the point spread function of the system according to their amplitude, area, and shape. Events that do not fit a single point spread function are likely due to either multiple detections or noise and were discarded after this comparison. The location of single isolated vaporized droplets was calculated by the “centroid” method.<sup>10</sup> The centroid of each localized vaporized droplet was computed by calculating the intensity weighted center of mass. The resulting super-resolution map was created from all the localizations detected over all the imaging frames.

The basic principle of acoustic wave sparsely activated localization microscopy (AWSALM) is that the first

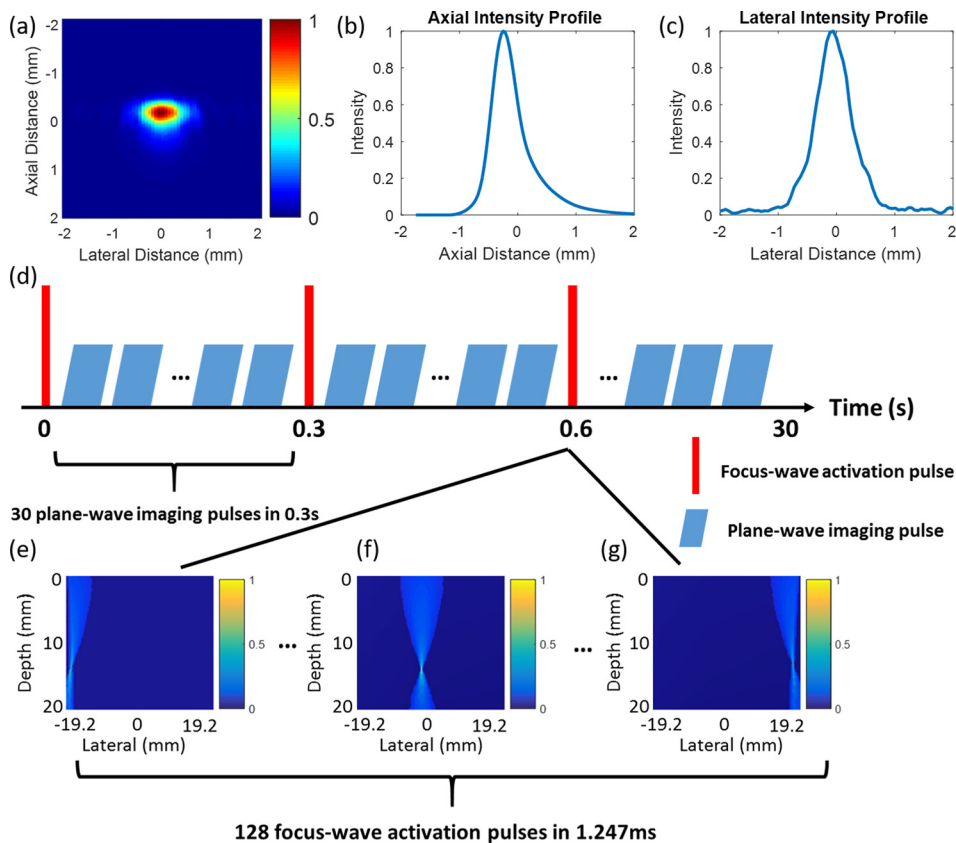


FIG. 1. (a)–(c) Characterization of ultrasound imaging system—Verasonics 128 research platform equipped with an L11-4v probe. (a) A representative frame of 50- $\mu$ m-diameter tube cross section imaged at a distance of 2 cm. Measurements of the full-width-half-maximum in the axial (b) and lateral (c) directions, respectively. (d) The illustration of customized “Activation-Imaging” ultrasound pulse sequence used. (e)–(g) show the normalized beam intensity profile of three different activation focus-pulses while scanning across the focal region. The maximum acoustic pressure is located at the pre-set focal depth = 15 mm.

activation pulse will sparsely activate a subgroup of nanodroplets as the activation pulse pressure is selected to only activate the largest most easily activated nanodroplets. These activated nanodroplets will generate acoustic signals until the next activation pulse.

From Fig. 2(a), it can be seen that, after activation, the number of localization events of vaporized droplets decreases over time. This is because a relatively high mechanical index imaging pulse was used, and therefore, the vaporized droplets were likely to undergo diffusion or coalescence under such an imaging acoustic pressure.<sup>27</sup> The SVD processing acts to filter out the static signal and keep the fluctuating signals. Thus, the movements of vaporized droplets in different imaging frames provide more localization events after each activation.

The second activation pulse will serve two purposes: first to destroy the existing vaporized nanodroplets generated

from the previous activation pulse, and second, to activate a new subgroup of nanodroplets. This continuous activation and subsequent imaging can provide localizations of different subgroups of vaporized nanodroplets. Figure 2(b) shows representative frames of localizations of vaporized nanodroplets after successive activations.

The sparse and apparently stochastic signals from activated nanodroplets, as shown in Fig. 2, may be due to a number of factors. A key factor is that the droplet population consists of droplets with a statistical distribution of different

TABLE I. “Activation-Imaging” pulse sequence and the corresponding ultrasound parameters used in the experiments. Peak-negative-pressure (PNP) represents the spatial and temporal peak-negative-pressure. Mechanical index is defined as the peak negative pressure of the acoustic wave (MPa) divided by the square root of center frequency of the acoustic wave (MHz).

State	Pulse type	Transmit frequency (MHz)	Pulse length (cycle)	PNP (MPa)	Mechanical index
Activation	Focus-pulse	8	2	3.68	1.30
Imaging	Plane-wave	4	1	0.50	0.25

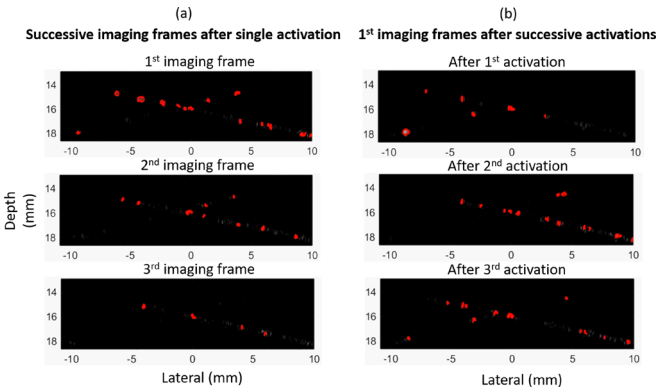


FIG. 2. (a) Representative image frames show the successive US image frames of vaporized nanodroplet signals after one activation. (b) Representative image frames show the first US image frame of vaporized nanodroplet signals acquired after successive activations. Multimedia view: <https://doi.org/10.1063/1.5029874.1>



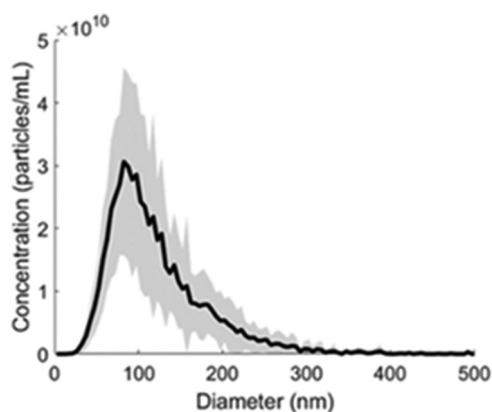


FIG. 3. The concentration and size distribution measurement of nanodroplet solution measured using a NanoSight NS300. The black line and shaded error bar represent the mean and standard deviation of concentration at each diameter, respectively.

size and shell properties. The size distribution of nanodroplets can be seen from Fig. 3, and the nanodroplets are poly-disperse with sizes ranging from about 50 to 300 nm. The droplet size and shell properties are important factors determining the acoustic pressure threshold required for vaporizing the droplets. According to Ref. 28, it was found that the activation threshold is inversely proportional to the size of a nanodroplet, which means that at a relatively low acoustic pressure, the relatively large droplets can be activated. The optical demonstration of droplet activation with increasing pressure has been shown previously.<sup>22</sup> Therefore, only a sparse subset of relatively large droplets randomly spatially distributed in the tube phantom are sensitive to the low activation pressure used here ( $MI = 1.3$ ), and the nanodroplets were regarded to be sparsely activated by the first activation pulse. The subsequent imaging pulses and next activation pulse will cause a large percentage of activated nanodroplets to be destroyed, including through shell rupture, diffusion, and dissolution.<sup>24,29</sup> The nanodroplets activated by the next activation pulse may be affected by a range of factors. First, they may be affected by any remaining nearby activated nanodroplets generated by the previous activation.<sup>22</sup> More specifically, the wave emitted from a vaporised droplet (following insonation from the second activation pulse) could be directional and have a random direction, and therefore, a nanodroplet experiencing this wave in addition to the second

activation pulse is likely to be activated more easily. Moreover, the non-linear distorted waves from nonlinear propagation and from vaporised droplets may also have superharmonics with wavelength close to the droplet size, thus contributing to the initiation of droplet activation by the next pulse.<sup>30</sup> Second, they may be affected by any increase in local temperature due to the activation and imaging pulses, as nanodroplets have a lower activation pressure as temperature increases.<sup>18</sup> Furthermore, it may be possible for the previous activation and imaging pulses to modify the droplets, making them easier to vaporize subsequently. Further research is required to determine which of these effects dominates and if other mechanisms are involved. Nevertheless, Fig. 2(b) demonstrates that new droplets are activated after each new activation pulse.

Figures 4(a)–4(c) show the localization of vaporized droplets at different activation pressure levels from  $MI = 1.3$  to 1.9. As the activation pressure level increases, there are more vaporized droplets. However, many of these vaporized droplets are not spatially isolated which introduces localization errors. As can be seen from Fig. 4(d), the number of total localization events increases from  $MI = 1.1$  until 1.4 where a plateau is reached. Although more nanodroplets are activated as the mechanical index of activation pulse increases, these vaporized nanodroplets may not be spatially isolated and therefore may not contribute to detected localization events that are useful for super-resolution imaging. As part of the post-processing, an algorithm was used to reject non-isolated bubble signals. It can be seen in Fig. 4(d) that the number of localization events after rejection increases until it plateaued at  $MI = 1.3$ , suggesting that this activation level may be optimal in providing spatially isolated signals for localization processing. The *in vivo* assessment of potential bio-effects from the low-boiling-point perfluorocarbon droplet activation has already been carried out by Nyankima.<sup>31</sup> It found that the decafluorobutane droplet activation at this moderate pressure level ( $MI = 0.81$ – $1.35$ ) will not induce any short-term or long-term bio-effects in the rodent kidney.

Figure 5 shows the evaluation results on the non-flow cross-tube phantom. In Fig. 5, two regions of interest (ROIs) were selected to measure the FWHM of the image of the tube. The left ROI is perpendicular to the tube and  $15^\circ$  tilted to the vertical plane. Each ROI has a width of 0.5 mm. Figure 5(d) shows that the FWHM value is  $210 \mu\text{m}$  for the super-resolution image whereas it is  $560 \mu\text{m}$  for the B-mode image. For the right-hand ROI, the B-mode image cannot distinguish the structure of two tubes but the FWHM measurement in super-resolution image shows that two tubes are  $210 \mu\text{m}$  apart as shown in Fig. 5(e).

In summary, this study is the demonstration of AWSALM, a super-resolution ultrasound imaging technique using acoustic activation and deactivation of nanodroplets at an acoustic pressure within the FDA-approved safety range. The much smaller size of the nanodroplets compared to microbubble contrast agents means that the technique can potentially super-resolve structures beyond the reach of the current microbubble based ultrasound super-resolution approaches. In addition, simultaneous sparse activation and deactivation of nanodroplets can potentially reduce the

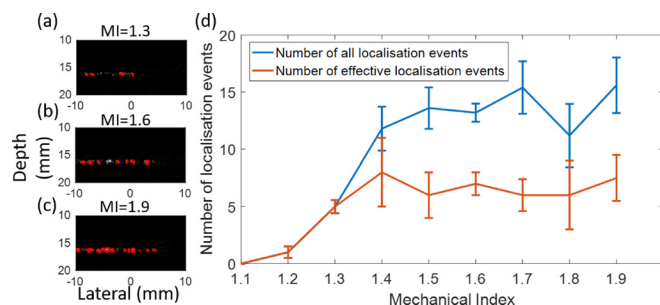


FIG. 4. Representative images show the visualization of localization of vaporized nanodroplets under mechanical indices of (a) 1.3, (b) 1.6, and (c) 1.9. (d) The number of all localization events and the localization events after rejection as the mechanical index of activation pulse increases.

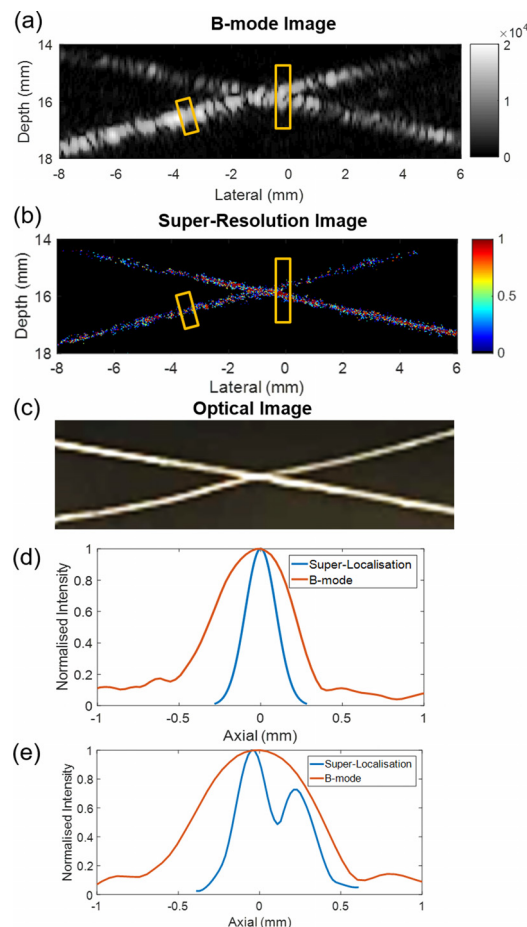


FIG. 5. (a) Conventional B-mode image displayed using a linear scale, (b) super-resolution image, and (c) optical image of the non-flow cross-tube phantom without any flow in the tubes. The left (d) and right (e) region of interests were chosen to compare FWHM measurements between the B-mode and super-resolution image.

acquisition time of super-resolution imaging compared to the time taken for conventional microbubble contrast agents to flow across the volume imaged. AWSALM is flow and concentration independent and has the potential to super-resolve micro-structures beyond the vasculature and also to reduce the imaging acquisition time compared to super-resolution imaging of conventional microbubble contrast agents flowing through microvasculature.

This research was partially funded by the UK EPSRC under Grant Nos. EP/N015487/1, EP/N014855/1, and EP/M011933/1, and the CRUK Multidisciplinary Project Award (No. C53470/A22353).

- <sup>1</sup>E. Betzig, G. H. Patterson, R. Sougrat, O. W. Lindwasser, S. Olenych, J. S. Bonifacino, M. W. Davidson, J. Lippincott-Schwartz, and H. F. Hess, *Science* **313**, 1642 (2006).
- <sup>2</sup>B. Dudok, L. Barna, M. Ledri, S. I. Szabo, E. Szabadits, B. Pinter, S. G. Woodhams, C. M. Henstridge, G. Y. Balla, R. Nyilas *et al.*, *Nat. Neurosci.* **18**, 75 (2015).
- <sup>3</sup>M. J. Rust, M. Bates, and X. Zhuang, *Nat. Methods* **3**, 793 (2006).
- <sup>4</sup>N. Clark, *Diabetes Care* **26**, 265 (2003).
- <sup>5</sup>P. G. Camici and F. Crea, *N. Engl. J. Med.* **356**, 830 (2007).
- <sup>6</sup>N. Weidner, *J. Pathol.* **184**, 119 (1998).
- <sup>7</sup>A. Stanzola, M. Toulemonde, Y. O. Yildiz, R. J. Eckersley, and M. X. Tang, *IEEE Signal Process. Mag.* **33**, 111 (2016).
- <sup>8</sup>D. Cosgrove, *Eur. J. Radiol.* **60**, 324 (2006).
- <sup>9</sup>O. M. Viessmann, R. J. Eckersley, K. Christensen-Jeffries, M. X. Tang, and C. Dunsby, *Phys. Med. Biol.* **58**, 6447 (2013).
- <sup>10</sup>K. Christensen-Jeffries, R. J. Browning, M. X. Tang, C. Dunsby, and R. J. Eckersley, *IEEE Trans. Med. Imaging* **34**, 433 (2015).
- <sup>11</sup>C. Errico, J. Pierre, S. Pezet, Y. Desailly, Z. Lenkei, O. Couture, and M. Tanter, *Nature* **527**, 499 (2015).
- <sup>12</sup>K. Christensen-Jeffries, J. Brown, P. Aljabar, M. Tang, C. Dunsby, and R. J. Eckersley, *IEEE Trans. Ultrason. Ferroelectr. Freq. Control* **64**, 1478 (2017).
- <sup>13</sup>M. A. O'Reilly and K. Hynynen, *Med. Phys.* **40**, 110701 (2013).
- <sup>14</sup>Y. Desailly, O. Couture, M. Fink, and M. Tanter, *Appl. Phys. Lett.* **103**, 174107 (2013).
- <sup>15</sup>F. Lin, S. E. Shelton, D. Espindola, J. D. Rojas, G. Pinton, and P. A. Dayton, *Theranostics* **7**, 196 (2017).
- <sup>16</sup>S. Lin, G. Zhang, C. H. Leow, and M.-X. Tang, *Phys. Med. Biol.* **62**, 6884 (2017).
- <sup>17</sup>P. S. Sheeran, J. D. Rojas, C. Puett, J. Hjelmquist, C. B. Arena, and P. A. Dayton, *Ultrasound Med. Biol.* **41**, 814 (2015).
- <sup>18</sup>P. S. Sheeran and P. A. Dayton, *Scientifica* **2014**, 579684.
- <sup>19</sup>G. Zhang, S. Lin, C. H. Leow, K. Pang, J. Hernández-Gil, M. Chee, N. J. Long, T. O. Matsunaga, and M. X. Tang, in IEEE International Ultrasonics Symposium (IUS) (2017).
- <sup>20</sup>T. Ji, Y. Zhao, Y. Ding, and G. Nie, *Adv. Mater.* **25**, 3508 (2013).
- <sup>21</sup>G. P. Luke, A. S. Hannah, and S. Y. Emelianov, *Nano Lett.* **16**, 2556 (2016).
- <sup>22</sup>P. S. Sheeran, T. O. Matsunaga, and P. A. Dayton, *Phys. Med. Biol.* **58**, 4513 (2013).
- <sup>23</sup>S. Lin, G. Zhang, C. H. Leow, O. T. Matsunaga, and M. X. Tang, in IEEE International Ultrasonics Symposium (2016).
- <sup>24</sup>S. Lin, G. Zhang, A. Jamburidze, M. Chee, C. H. Leow, V. Garbin, and M. X. Tang, *Phys. Med. Biol.* **63**, 065002 (2018).
- <sup>25</sup>G. Montaldo, M. Tanter, J. Bercoff, N. Benech, and M. Fink, *IEEE Trans. Ultrason. Ferroelectr. Freq. Control* **56**, 489 (2009).
- <sup>26</sup>J. Brown, K. Christensen-Jeffries, S. Harput, C. Dunsby, M. X. Tang, and R. J. Eckersley, IEEE International Ultrasonics Symposium (2017).
- <sup>27</sup>J. L. Raymond, Y. Luan, T. Peng, S. L. Huang, D. D. McPherson, M. Versluis, N. de Jong, and C. K. Holland, *Phys. Med. Biol.* **61**, 8321 (2016).
- <sup>28</sup>P. S. Sheeran, V. P. Wong, S. Luo, R. J. McFarland, W. D. Ross, S. Feingold, T. O. Matsunaga, and P. A. Dayton, *Ultrasound Med. Biol.* **37**, 1518 (2011).
- <sup>29</sup>N. Y. Rapoport, A. L. Efros, D. A. Christensen, A. M. Kennedy, and K.-H. Nam, *Bubble Sci., Eng., Technol.* **1**, 31 (2009).
- <sup>30</sup>O. Shpak, M. Verweij, H. J. Vos, N. de Jong, D. Lohse, and M. Versluis, *Proc. Natl. Acad. Sci. U. S. A.* **111**, 1697 (2014).
- <sup>31</sup>A. G. Nyankima, J. D. Rojas, R. Cianciolo, K. A. Johnson, and P. A. Dayton, *Ultrasound Med. Biol.* **44**, 368 (2018).